This is the peer-reviewed, final accepted version for American Mineralogist, published by the Mineralogical Society of America.
The published version is subject to change. Cite as Authors (Year) Title. American Mineralogist, in press.
DOI: https://doi.org/10.2138/am-2022-8746. http://www.minsocam.org/

Revision 2

Compositional trends in Ba-, Ti-, and Cl-rich micas from metasomatized mantle rocks of the Gföhl Unit, Bohemian Massif, Austria

Tereza Zelinková[1,*], Martin Racek[1], Rainer Abart[2]

[1] Institute of Petrology and Structural Geology, Charles University, Albertov 6, 128 43 Prague 2, Czech Republic

[2] Department of Lithospheric Research, University of Vienna, Josef-Holaubek-Platz 2, 1090 Vienna, Austria

*Email: tereza.zelinkova@natur.cuni.cz

ABSTRACT

Ba-, Ti-, and Cl-rich micas associated with other Ba- and/or Cl-rich minerals in the rock matrix or in garnet and clinopyroxene hosted multiphase solid inclusions (MSI) are observed in mantle-derived garnet pyroxenites. The micas show extremely high variability in chemical composition ranging between Ba-rich phlogopite, chloroferrokinoshitalite, and oxykinoshitalite. Elemental covariation trends in mineral chemical data reveal the principal substitution mechanisms responsible for the observed chemical variability. The substitution $Ba^{2+}Al^{3+}\leftrightarrow K^{1+}Si^{4+}$ associated with either $OH^{1-}\leftrightarrow Cl^{1-}$ or $Ti^{4+}2O^{2-}\leftrightarrow Mg^{2+}2OH^{1}$ links phlogopite to chloroferrokinoshitalite and oxykinoshitalite, respectively, whereas the substitution $Ti^{4+}2O^{2-}\leftrightarrow Fe^{2+}2Cl^{1-}$ links chloroferrokinoshitalite to oxykinoshitalite. The preferred incorporation of Cl in Fe-rich mica and of Ti+O in Mg-rich mica indicates that XFe (Fe_{tot}/Fe_{tot}+Mg) exerts an important control on mica composition. The positive correlation of XFe with Cl led to the formation of possibly the most Cl-rich mica so far described classified as chloroferrokinoshitalite ($XFe_{0.88}$, $Ba_{0.95}K_{0.03}Fe_{2.68}Mg_{0.37}Al_{1.91}Si_{2.01}Cl_{1.98}$) with 10.98 wt% Cl. Substantial substitution of OH^- by Cl^- and

This is the peer-reviewed, final accepted version for American Mineralogist, published by the Mineralogical Society of America.
The published version is subject to change. Cite as Authors (Year) Title. American Mineralogist, in press.
DOI: https://doi.org/10.2138/am-2022-8746. http://www.minsocam.org/

O^{2-} in mica, and the presence of Cl-apatite, a rare Cl-rich phosphate goryainovite, and carbonates together with Cl-rich micas indicate high Cl and CO_2 activity and low H_2O activity in metasomatizing fluids or melts that may be classified as Ba-Cl-rich silicocarbonatitic. The coexistence of two micas with distinct compositions close to chloroferrokinoshitalite ($XFe_{0.57–0.77}$, $K{\sim}_{0.1}Ba_{0.6–0.8}Mg_{0.7–1.3}Fe_{1.7–2.3}Ti_{0.0–0.1}Si_{2.2–2.3}Al_{1.5–1.7}Cl_{1.2–1.8}$) and oxykinoshitalite ($XFe_{0.19–0.20}$, $K_{\sim0.3}Ba_{\sim0.5}Mg_{2.0–2.1}Fe_{\sim0.5}Ti_{0.2–0.4}Si_{2.4–2.6}Al_{\sim1.8}Cl_{\sim0.3}$) suggests that a miscibility gap exists between these two compositions. The exotic mineral assemblage was formed by interaction with metasomatizing fluids or melts whose origin cannot be defined with certainty. They may be derived from crustal or mantle lithologies or from the host garnet pyroxenites. The textural position of the MSI in garnet and their characteristic mineral assemblages indicate that they have been introduced into the garnet crystals under post-peak conditions, possibly during decompression. With this research we document substitution mechanisms in Ba-, Ti-, and Cl-rich micas and shed light on the behavior and composition of fluids or melts at the upper mantle/lower crust interface.

Keywords: garnet pyroxenite, metasomatism, multiphase solid inclusions, fluids, melts, kinoshitalite

INTRODUCTION

Occurrence and origin of Ba- (Cl-) bearing micas

Ba- and Cl-rich mineral assemblages including Ba-rich micas have been documented from a wide range of crustal lithologies including ore deposits (Pattiaratchi et al. 1967; Jiang et al. 1996; Gnos and Armbruster 2000), banded iron-formations (Henry and Daigle, 2018; Kullerud, 1995), metacherts (Grapes 1993), metaexhalites (Oen and Lustenhouwer 1992), magnetite bearing gneisses (Léger et al., 1996), skarns and marbles (Bol et al. 1989; Tracy 1991), charnockites and related rocks (Kamineni et al. 1982; Sharygin et al. 2014), olivine nephelinite

(Kogarko et al., 2005; Manuella et al., 2012), and MORB derived amphibolite and associated lithologies (Blanco-Quintero et al., 2011). Their formation is mainly related to infiltration of metasomatizing fluid or melt, which may be derived from barite-bearing sediments (e.g. Grapes, 1993; Tracy, 1991), or to hydrothermal alteration of the rocks by fluids or melts associated with ore formation (e.g. Jiang et al., 1996; Henry and Daige, 2018). In magmatic rocks, they may originate from melting of enriched/metasomatized mantle (Kogarko et al. 2005, 2007; Manuella et al. 2012; Lopes and Ulbrich 2015) or from subducted MORB infiltrated by Ba(-Cl) fluids or melts (Blanco-Quintero et al. 2011).

In mantle lithologies, Ba(-Cl)-rich micas and other Ba(-Cl)-rich phases are rare, but they are known from the matrix of garnet peridotite (Tumiati et al. 2007). These phases specifically occur within multiphase solid inclusions, henceforth referred to as MSI, in garnet or spinel from (U)HP garnet pyroxenites, eclogites, peridotites, and chromitites (Zaccarini et al. 2004; Faryad et al. 2010; Borghini et al. 2018, 2020; Čopjaková and Kotková 2018; Naemura et al. 2018; Kotková et al. 2021).

In general, MSI are a type of inclusion up to 100 μm in size interpreted as fluid or melt trapped in crystals during their initial growth or during healing of cracks in preexisting crystals. In crustal lithologies, MSI may occur as so called nanogranites (Cesare et al. 2011; Ferrero et al. 2015a, 2015b). MSI occur mostly in peak mineral assemblages of (U)HP and (U)HT rocks and are comprised of hydrous aluminosilicate minerals including micas, anhydrous silicates and carbonates, whereas sulfates, sulfides, phosphates, and oxides are less common. Very rarely MSI contain diamond and/or graphite (Frezzotti and Ferrando 2015 and references therein).

In mantle rocks, Ba(-Cl)-bearing micas are often associated with other silicate, carbonate, and phosphate minerals and are usually interpreted as a result of interaction with metasomatizing

This is the peer-reviewed, final accepted version for American Mineralogist, published by the Mineralogical Society of America.
The published version is subject to change. Cite as Authors (Year) Title. American Mineralogist, in press.
DOI: https://doi.org/10.2138/am-2022-8746. http://www.minsocam.org/

LILE and Cl-rich, sometimes potassic carbonatitic fluids or melts derived from a subducting crustal slab (Faryad et al. 2013, Naemura et al. 2018). Furthermore, the metasomatizing agent may be enriched in Mg, Fe, Al, and Cr derived from rocks in the mantle wedge (Tumiati et al. 2007; Naemura et al. 2009, 2018; Borghini et al. 2018, 2020; Čopjaková and Kotková 2018; Kotková et al. 2021).

Trioctahedral Ba(-Cl) bearing micas

The basic building blocks of the crystal structure of mica are represented by layers comprised of one central sheet of octahedrally coordinated cations sandwiched between two sheets of tetrahedrally coordinated cations. The three-sheet layers have a net negative charge and are held together by interlayer cations. A simplified formula of mica can be written as $I\ M^{VI}_{2-3}\ \square_{1-0}\ T^{IV}_4\ O_{10}\ A_2$, where I represents interlayer cations (Cs^{1+}, K^{1+}, Na^{1+}, NH_4^{1+}, Rb^{1+}, Ba^{2+}, Ca^{2+}); M represents octahedrally coordinated cations (Li^{1+}, $Fe^{2+,}$ Fe^{3+}, Mg^{2+}, Mn^{2+}, Mn^{3+}, Zn^{2+}, Al^{3+}, Cr^{3+}, V^{2+}, V^{3+}, Ti^{4+}); □ represents a vacancy; T represents tetrahedrally coordinated cations (Be^{2+}, Al^{3+}, B^{3+}, Fe^{3+}, Si^{4+}); A represents anions (Cl^{1-}, F^{1-}, OH^{1-}, O^{2-}, S^{2-}) (Rieder et al. 1999). Of the octahedrally coordinated lattice sites, two thirds may be filled with trivalent cations or all octahedrally coordinated lattice sites may be filled with divalent cations, giving rise to dioctahedral and trioctahedral micas, respectively.

In trioctahedral micas, K–Ba substitution at the interlayer I position connects the phlogopite-annite series with Ba-micas and is coupled with Al–Si substitution at the T position: $Ba^{2+}+Al^{3+}\leftrightarrow(K^{1+},Na^{1+})+Si^{4+}$ (Tischendorf et al., 2007). If the Ba content exceeds 0.5 atoms per formula unit (a.p.f.u.), the mica is classified as kinoshitalite (Mg-rich end member) or ferrokinoshitalite, where Mg is replaced by Fe in the M position (Guggenheim and Frimmel

1999). In oxykinoshitalite, the K–Ba substitution is accompanied by the exchange $Ti^{4+}+2O^{2-} \leftrightarrow Mg^{2+}+2(OH,F)^{1-}$ (Kogarko et al., 2005). With increasing Cl content on the A position, the transition from ferrokinoshitalite to chloroferrokinoshitalite occurs. Mica with a composition of chloroferrokinoshitalite with Cl occupying more than 0.5 of the A position was previously described (Tracy 1991), although it was misidentified as anandite - Ba-bearing mica that contains predominantly S on the A position (Filut et al., 1985; Pattiaratchi et al., 1967). Another Ba-rich dioctahedral brittle mica is chernykhite, where the M position is rich in V (Ankinovich et al. 1973). The composition of the micas mentioned above and the assignments to structural positions are shown in Table 1.

In this work, we document the occurrence of Ba(-Cl)-rich trioctahedral micas and related exotic phases including Cl-rich phosphates with carbonates and other silicate phases in MSI hosted by garnet and clinopyroxene as well as in the matrix of mantle-derived garnet pyroxenites. Detailed evaluation of a large set of mica analyses involving compositions so far not described from natural samples allows identification of the main substitution mechanisms and compositional correlations that help to better constrain the factors controlling such uncommon mica compositions. The study of mineral assemblages extremely enriched in Ba, Cl, and CO_2 can shed light on the character of metasomatic agents that affect mantle rocks during orogenic processes.

GEOLOGICAL SETTING

The garnet pyroxenites in this study were collected in the St. Leonhard and Dunkelsteiner Wald granulite massifs located in Lower Austria. Both massifs are part of the Gföhl Unit of the Moldanubian Domain of the Bohemian Massif (Figure 1; e.g. Schulmann et al., 2008). According

115 to recent interpretations, the granulite massifs of the Gföhl Unit were derived from the
116 Saxothuringian plate, which was subducted to mantle depth beneath the Teplá-Barrandian plate.
117 Subsequently, the crustal material was underplated beneath the orogenic root and later exhumed
118 due to the indentation of the Brunia microcontinent under the Moldanubian Domain (Racek et al.
119 2006; Guy et al. 2011; Schulmann et al. 2014; Kusbach et al. 2015; Maierová et al. 2021)

120 The granulite massifs from the Saxothuringian Domain and the Gföhl Unit are
121 predominantly formed by felsic kyanite and K-feldspar bearing granulites and gneisses, but they
122 also contain a large number of garnet peridotite bodies associated with layers or lenses of garnet
123 pyroxenites and eclogites. These latter rocks are interpreted as mantle fragments that were
124 incorporated into the continental crust during or after the subduction of the Saxothuringian plate
125 under the Teplá-Barrandian plate during the Variscan orogeny (Cooke 2000; Medaris et al. 2005;
126 Schmädicke et al. 2010; Kusbach et al. 2015). Multiple genetic models have been proposed for
127 garnet pyroxenites and eclogites occurring within garnet peridotites of the Gföhl and
128 Saxothuringian granulite massifs, including: 1) HT-HP crystallization from silicate melts
129 containing components of the oceanic crust (Medaris et al., 1995; Medaris et al., 2013); 2) high
130 pressure cumulates of hot melts derived from the asthenosphere (Becker 1997; Schmädicke et al.
131 2010); and 3) metasomatism of peridotites by melts derived from a phengite-bearing protolith
132 already present in the peridotites or more probably within the deeply subducted continental crust
133 (Borghini et al. 2018, 2020). Furthermore, mafic and intermediate granulites sometimes occur in
134 association with pyroxenite bodies at the contact with felsic granulites (Cooke, 2000; Petrakakis
135 et al., 2018; Racek et al., 2008).

136 Using thermodynamic modelling or thermobarometry, the maximum P-T conditions were
137 estimated to be 11–25 kbar and 750–1200 °C for the felsic granulites, 16–25 kbar and 1050–1200

°C for the intermediate granulites, and 11–19 kbar and 800–1090 °C for the mafic granulites (Gayk et al. 1995; Štípská and Powell 2005; Medaris et al. 2006; Racek et al. 2006, 2008). The occurrence of microdiamond and coesite inclusions in the felsic granulites shows that at least some of these granulites underwent metamorphism under UHP conditions of 850–1100 °C and ~45 kbar (Kotková et al., 2021; Kotková et al., 2011; Perraki and Faryad, 2014). For garnet peridotites, peak metamorphic conditions of 20–60 kbar and 900–1400°C were estimated (Carswell 1991; Medaris et al. 2005; Schmädicke et al. 2010). Equilibration conditions for garnet pyroxenite associated with peridotite from the Gföhl Unit have been estimated to be ~900 °C and 22–37 kbar (Faryad et al., 2009; Medaris et al., 2013). However, some garnet pyroxenites contain relics of a primary coarse grained texture that was formed at 22–25 kbar and 1300–1400 °C and was later overprinted at considerably higher pressure of 45–50 kbar, and lower temperature of 1100 °C (Faryad et al. 2009).

The decompression conditions for felsic, intermediate, and mafic granulites have been estimated to be 5–13 kbar and 650–910 °C (Cooke, 2000; Racek et al., 2008; Štípská et al., 2004; Petrakakis et al. 2018), for peridotites with garnet pyroxenites 12–13 kbar and 840–860 °C were estimated (Schmädicke et al. 2010), and for eclogites 18–20 kbar and 835–935 °C were obtained (Medaris et al., 2006).

SAMPLES AND METHODS

Mineral assemblages involving Ba- and Cl- rich phases were documented in ten polished thin sections of garnet pyroxenites collected from five localities. The respective GPX coordinates are given in Online Materials (Table OM1 in file Supp1).

This is the peer-reviewed, final accepted version for American Mineralogist, published by the Mineralogical Society of America.
The published version is subject to change. Cite as Authors (Year) Title. American Mineralogist, in press.
DOI: https://doi.org/10.2138/am-2022-8746. http://www.minsocam.org/

Backscattered electron (BSE) images, compositional maps, and electron probe microanalyses were acquired using a Jeol JXA-8530F electron probe microanalyzer at the Institute of Petrology and Structural Geology (Faculty of Science, Charles University, Prague, Czech Republic). The following conditions were used for quantitative microanalysis: micas were analyzed with an accelerating voltage of 15 kV and a probe current of 12 nA with the electron beam defocused to 2–5 μm (depending on crystal size); phosphates and carbonates were analyzed at 15 kV and 10 nA with the electron beam defocused to 2–5 μm; garnet was analyzed at 15 kV and 40 nA with a focused 1 micron electron beam spot; other minerals were analyzed at 15 kV and 20 nA with the electron beam defocused to 2–5 μm for scapolite and plagioclase and focused for other phases. The following standards consisting of natural or synthetic phases with certified compositions were used for quantitative analyzes: topaz (F), albite (Na), periclase (Mg), corundum (Al), quartz (Si), apatite (P), anhydrite (S), tugtupite (Cl), sanidine (K), diopside (Ca), rutile (Ti), vanadium (V), chromium oxide (Cr), rhodonite (Mn), magnetite (Fe), willemite (Zn), celestite (Sr), baryte (Ba), LaP_5O_{14} (La), and CeP_5O_{14} (Ce). Kα lines of the characteristic X-rays were used for detection and quantification of all elements, except for Ba, Sr, La, and Ce where Lα lines were used. The ZAF method was applied for matrix correction. Due to the interference of the Ti Kα and Ba Lα peaks, correction of the peak intensities was performed based on the coefficients defined by the analysis of the Ti and Ba standards (rutile and baryte). Compositional maps were acquired with an accelerating voltage of 20 kV, a probe current of 150 nA, a beam spot size of 1 micron, a step size of 10 μm, and a dwell time of 35 ms per point.

Chemical analyzes of garnet were calculated to 12 oxygens/8 cations, pyroxenes on 6 oxygens/4 cations, feldspar on 8 oxygens/5 cations, spinel on 4 oxygens/3 cations, apatite on 12.5 oxygens/8 cations, goryainovite on 4.5 oxygens/3 cations, cordierite on 18 oxygens/11 cations,

183 sapphirine on 20 oxygens/14 cations and margarite on 11 oxygens/7cations. Amphiboles were
184 calculated on 23 oxygens with the methodology of Locock (2014) modified by the addition of
185 BaO to oxides, and the recalculated Fe was considered to be all Fe^{2+}. Scapolite was normalized to
186 (Si+Al)=12 a.p.f.u after Teertstra & Sherriff (1997). Micas that form solid solutions between
187 phlogopite/annite and Ba-bearing trioctahedral micas contain 8 cations, but their charge is not
188 constant. While most end members have charge 22, oxykinoshitalite has charge 24 due to the OH^-
189 $\leftrightarrow O^{2-}$ substitution. Therefore, all Ba-bearing mica analyzes were recalculated to 8 cations.

190 Representative chemical analyzes of Ba-, Ti-, and Cl- rich micas are given in Table 2 and
191 representative chemical analyzes of phosphates are given in Table 3. Other chemical analyzes are
192 given in Online Materials (Tables OM2-OM4 in file Supp1): peak and secondary associations in
193 garnet pyroxenites, Table OM2; all analyses of Ba-, Ti-, and Cl- rich micas, Table OM3; and
194 silicates, and carbonates in MSI, Table OM4. A total of 100 mica analyzes were taken, 22 from
195 micas in the matrix, 73 from micas hosted by garnet and 5 from MSIs hosted by clinopyroxene.

196 All Fe is expressed as Fe^{2+}. The notation used to describe mineral compositions is as follows:
197 $XFe=Fe_{tot}/(Fe_{tot}+Mg)$, $Jd=Na/(Na+Ca)*100$, $Ab=Na/(Na+K+Ca)*100$,
198 $CaTs=Al_T*Ca_{M2}/(Mg+Fe+Mn+Ca)_{M2}*100$, $Prp=Mg/(Mg+Fe+Ca+Mn)*100$,
199 $Alm=Fe/(Fe+Mg+Ca+Mn)*100$, $Grs=Ca/(Ca+Fe+Mg+Mn)*100$, and
200 $Sps=Mn/(Mn+Fe+Mg+Ca)*100$. The recalculation of cations/anions in the structural positions of
201 the micas, (Online Materials Table OM3 in file Supp1): $TAl=Al-(Al+Si-4)$, $IAl=(Si+Al-4$;
202 values less than $0 \rightarrow 0$), $O=Ti*2$, and $OH=2-Cl-F-O$.

203 Mineral abbreviations are taken from Whitney and Evans (2010), except for the abbreviation for
204 the studied micas (Mca), which are taken from Siivola and Schmid (2007).

205

206 # RESULTS

207 ## Sample description

208 Although the garnet pyroxenites come from different localities, they generally show a
209 common feature in the form of remnants of the primary mineral assemblage comprising garnet
210 porphyroblasts with rare inclusions of clinopyroxene and kyanite, and preserved clinopyroxene
211 grains in a fine to medium-grained matrix (Figure 2a). The presence and abundance of individual
212 mineral phases varies in different samples. Common accessory phases include sulphides (mainly
213 pyrite, chalcopyrite, and pentlandite) and rutile partly replaced by ilmenite. Retrogression of the
214 pyroxenites led to the formation of variable amounts of plagioclase, clinopyroxene,
215 orthopyroxene, and amphibole in the form of coarse-grained and sometimes also fine-grained
216 symplectites. The symplectites are mostly formed at the margins of the garnet porphyroblasts or
217 between grains of clinopyroxene in the matrix (Figures 2a, b) and are accompanied by spinel and
218 rarely by sapphirine. Importantly, Ba- and Cl-rich silicates, including micas and phosphate
219 minerals, are present in the matrix as single grains most often in fine-grained symplectites at the
220 contact with garnet, or they occur in small garnet-hosted MSI together with carbonates. More
221 rarely, they can also be found in MSI hosted by clinopyroxene that typically also show
222 orthopyroxene exsolution lamellae.

223 Detailed petrographic descriptions of individual samples including information on the
224 chemical composition and zoning of the main rock-forming minerals are given in Online
225 Materials (file Supp2).

Mineral chemistry of the peak assemblage. Garnet is generally dominated by pyrope, with considerable amounts of almandine and grossular components, while the spessartine content is negligible. In the samples studied, the composition range of garnet is $Py_{39.9–72.1}Alm_{14.6–34.7}Grs_{9.3–36.4}Sps_{0.3–1.6}$, $XFe_{0.17–0.41}$ (Online Materials Table OM2 in file Supp1). There is some variation in the character of the chemical zoning between samples, but in some cases also between individual garnet crystals within one sample (see Online Materials file Supp2). These variations are mainly related to the grossular content. While some garnets have grossular-rich cores and show a decrease of the grossular content toward the rims accompanied by an increase in the almandine and pyrope contents, other garnets, with a lower grossular content, have much less pronounced zoning. In some cases a slight increase in the grossular contents can be observed towards the rims accompanied by an increase in the almandine and a decrease in the pyrope content. Interestingly, the location of garnet hosted MSIs does not appear to correlate with the compositional zoning of the garnet.

The preserved clinopyroxene grains in the matrix are characterized by a core to rim decrease of Na and an increase in Ca contents. The compositional range of clinopyroxene from the matrix is: $CaTs_{5.0–13.2}Jd_{5.1–22.7}XFe_{0.11–0.16}$, $Al_{0.3–0.4}$ (a.p.f.u). Automorphic inclusions of clinopyroxene in the garnets have compositions of $CaTs_{4.0–14.2}Jd_{4.3–29.0}XFe_{0.06–0.14}$, $Al_{0.2–0.5}$ (a.p.f.u) (Online Materials Table OM2 in file Supp1).

Mineral chemistry of the retrograde assemblage. Clinopyroxene has compositions of $CaTs_{4.2–16.3}Jd_{3.8–12.2}XFe_{0.07–0.13}$. Orthopyroxene has close to enstatite composition: $XFe_{0.09–0.16}$, $Al_{0.1–0.3}$ (a.p.f.u). In plagioclase, the albite component predominates over the anorthite component: $Ab_{56.5–63.0}$. Amphibole has a pargasitic composition with $XFe_{0.10–0.19}$, $Ba_{0.0–0.1}Ti_{0.1–0.2}Cl_{0.0–0.4}Si_{5.9–6.1}$ (a.p.f.u). Spinel has a negligible Cr content: $XFe_{0.13–0.30}$, $Al_{1.9–2.0}Cr_{0.0–0.1}$ (a.p.f.u).

Sapphirine has $XFe_{0.06–0.07}$. Representative chemical compositions of these phases are given in Online Materials (Table OM2 in file Supp1).

Ba-Cl-rich mineral phases in the matrix. Ba-rich mica associated with celsian and Cl-rich apatite is present in the matrix, where it is mostly in contact with garnet (Figures 3a, b, c) and forms relatively large crystals, up to 0.3 mm in size. In some cases, this mica shows compositional zoning, which can be inferred from the relatively bright BSE contrast at the rims and the brightness variations across the cleavage (Figures 3a, b).

The compositional range of Ba-rich micas in the matrix is $XFe_{0.07–0.21}$, $K_{0.5–0.7}Ba_{0.1–0.3}Mg_{1.9–2.4}Fe_{0.2–0.5}Ti_{0.2–0.4}Si_{2.5–2.8}Al_{1.5–1.7}Cl_{0.0–0.1}$ (a.p.f.u) (Table 2, Online Materials Table OM3 in file Supp1). Domains with relatively bright BSE contrast are rich in Fe, Ba, and Cl with representative compositions of $XFe_{0.21}$, $K_{0.5}Ba_{0.3}Mg_{1.9}Fe_{0.5}Ti_{0.4}Si_{2.6}Al_{1.6}Cl_{0.0}$ (a.p.f.u) compared to domains with comparatively dark BSE contrast, where compositions are $XFe_{0.15}$, $K_{0.7}Ba_{0.1}Mg_{2.1}Fe_{0.4}Ti_{0.3}Si_{2.7}Al_{1.5}Cl_{0.0}$ (a.p.f.u). Apatite with compositions in the range of $Ca_{4.8–4.9}Sr_{0.0–0.1}P_{3.0–3.0}Cl_{0.5–0.7}F_{0.1–0.2}$ (a.p.f.u) corresponds to a solid solution between hydroxyapatite and Cl-apatite with a low F content (Table 3). Celsian has compositions of $Ba_{0.7–0.9}K_{\sim0.1}Ca_{0.0–0.1}Na_{0.0–0.1}Al_{\sim1.8}Si_{\sim2.1}$(a.p.f.u) (Online Materials Table OM2 in file Supp1).

Ba-Cl-rich mineral phases in clinopyroxene. Ba-mica and Cl-apatite are present as inclusions in clinopyroxene or are found in association with orthopyroxene exsolution lamellae (Figure 3d, e, f, g). In some cases, graphite is also present in these multiphase inclusions (Figure 3e).

The micas have compositions of $XFe_{0.21–0.30}$, $K_{\sim0.4}Ba_{0.4–0.5}Mg_{1.8–2}Fe_{0.5–0.8}Ti_{0.3–0.4}Si_{2.5–2.6}Al_{1.5–1.6}Cl_{0.2–0.3}$ (a.p.f.u) (Table 2, Online Materials Table OM3 in file Supp1). Apatite with

This is the peer-reviewed, final accepted version for American Mineralogist, published by the Mineralogical Society of America.
The published version is subject to change. Cite as Authors (Year) Title. American Mineralogist, in press.
DOI: https://doi.org/10.2138/am-2022-8746. http://www.minsocam.org/

compositions of $Ca_{4.7–4.8}Sr_{\sim0.1}P_{2.9–3.0}Cl_{0.9–1.0}F_{\sim0.0}$ (a.p.f.u) corresponds to chlorapatite with a minor hydroxyapatite component and a negligible F content (Table 3). Orthopyroxene exsolution lamellae associated with mica have compositions of $XFe_{\sim0.14}$, $Al_{\sim0.1}$ (a.p.f.u). Amphibole associated with mica in MSI has a pargasitic composition with $XFe_{\sim0.16}$, $Ba_{\sim0.0}Ti_{\sim0.2}Cl_{\sim0.5}Si_{\sim6.3}$ (a.p.f.u) (Online Materials Table OM4 in file Supp1).

Garnet-hosted polyphase inclusions containing Ba-Cl-rich minerals. Inclusions rich in carbonate minerals such as dolomite, calcite, and magnesite often form narrow chains crosscutting garnet crystals (Figure 4). Carbonate-rich inclusions are up to 15 μm in size and often have a hexagonal shape, indicating that they have a negative crystal shape controlled by the host garnet. They are sometimes accompanied by 3–60 μm sized MSIs, which are dispersed across all parts of the garnet. They do not form clusters (Figure 4a) or show any kind of systematic relation to the garnet zones (core or rim) nor do they correlate with the compositional zoning of garnet. Common mineral phases in these inclusions are Cl-rich apatite, monazite, dolomite, magnesite, amphibole, orthopyroxene, clinopyroxene, spinel, and Ba- (Ti-, Cl-) rich mica. Rarely, scapolite, aspidolite, cordierite, muscovite, goryainovite, celsian, norsethite, scheelite, epidote, and SiO_2 and Al_2SiO_5 polymorphs occur in these MSIs. All these phases can occur in various combinations and form intergrows with each other (Figure 4b, c, d, e, f, g, h, i, j).

Orthopyroxene is rich in enstatite with $XFe_{0.07–0.11}$, $Al_{\sim0.2}$ (a.p.f.u). Clinopyroxene is highly variable in composition and can locally contain considerably elevated amounts of Na and Al. Its composition mostly corresponds to the range from augite to diopside to omphacite: $CaTs_{3.9–20.5}Jd_{3.2–25.3}XFe_{0.08–0.20}$. In spinel, Al-end members prevail with $XFe_{0.20–0.49}$, $Al_{0.9–2.0}Cr_{\sim0.0}$ (a.p.f.u). The compositional range of amphibole varies from sadanagait to tschermakite to

pargasite: $XFe_{0.09–0.30}$, $Ba_{0.0–0.2}Ti_{0.1–0.3}Cl_{0.1–0.8}Si_{5.4–6.1}$ (a.p.f.u). The other phases have the following compositions: cordierite: $XFe_{\sim0.29}$, scapolite: $K_{\sim0.0}Na_{\sim0.7}Ca_{\sim3.0}Cl_{\sim0.2}Al_{\sim5.2}Si_{\sim6.8}$ (a.p.f.u), margarite: $Ca_{\sim0.7}Na_{\sim0.2}K_{\sim0.0}$ (a.p.f.u.), and celsian: $Ba_{0.7–0.9}K_{0.0–0.1}Ca_{\sim0.0}Na_{0.0–0.1}Si_{2.0–2.2}Al_{1.8–1.9}$ (a.p.f.u). Their representative chemical compositions are given in Online Materials Table OM4 in file Supp1.

Apatite has a composition of $Ca_{4.5–5.0}Sr_{0.0–0.5}P_{2.8–3.0}Cl_{0.2–1.1}F_{0.0–0.3}$ (a.p.f.u). With an average content of $Cl_{0.8}$ a.p.f.u., and can be classified as chlorapatite. The compositional range of goryainovite is $Ca_{1.9–2.0}Sr_{0.0–0.1}P_{\sim1.0}Cl_{0.7–0.8}$ (a.p.f.u). The highest Sr content in goryainovite is 2.5 wt% (Table 3).

Micas from MSI have compositions in the range $XFe_{0.08–0.94}$, $K_{0.0–0.6}Ba_{0.1–0.9}Mg_{0.2–2.4}Fe_{0.2–2.7}Ti_{0.0–0.9}Si_{2.0–2.9}Al_{1.5–2.1}Cl_{0.0–2.0}$ (a.p.f.u) (Table 2, Online Materials Table OM3 in file Supp1), where Ba predominates over K. They are enriched in Cl or Ti. Further details on the compositional correlations in mica are presented in the discussion.

Chemical analyzes for the norsethite, scheelite, aspidolite, muscovite, epidote and Al_2SiO_5 polymorph are not given, because they were too small for quantitative analysis, although they were identified based on energy dispersive spectra (EDS).

DISCUSSION

Substitution mechanisms and compositional correlations in micas

The chemical compositions of all micas analyzed (Online Materials Table OM3 in file Supp1) are plotted in element covariation diagrams, where various substitution trends and correlations are visible with regard to XFe and microstructural position (Figure 5). Additional

315 elemental covariation diagrams showing the correlations of multiple elements with XFe and Ba
316 contents are available in the Online Materials (file Supp3).

317 **$Ba^{2+}Al^{3+}\leftrightarrow K^{1+}Si^{4+}$ substitution.** This substitution is inferred from the negative
318 correlation of Ba with Si and K and from the positive correlation of Ba with Al (Figure 6). A
319 coupled substitution is required to maintain charge balance. This substitution links Ba-free end
320 members such as phlogopite to micas bearing Ba such as kinoshitalite, ferrokinoshitalite,
321 chloroferrokinoshitalite, or oxykinoshitalite. The structural formulae of all mica end members are
322 shown in Table 1. The $Ba^{2+}Al^{3+}\leftrightarrow K^{1+}Si^{4+}$ substitution has already been described in previous
323 works (e.g. Čopjaková and Kotková, 2018; Grapes, 1993; Kogarko et al., 2005).

324 **$Ti^{4+}2O^{2-}\leftrightarrow(Fe,Mg)^{2+}2(OH,Cl)^{1-}$substitution.** This substitution is inferred from the fact
325 that some mica analyses show variably elevated Ti contents of up to 12.55 wt% TiO_2
326 corresponding to 0.87 a.p.f.u. Ti (Table 2). The Ti content is negatively correlated with the total
327 of Mg+Fe, while there is no correlation of Ti with Si and Al. The slope of the correlation between
328 Ti and Mg+Fe is close to -1 over almost the entire range of the observed Ti contents. Only at the
329 lowest Ti content below 0.1 a.p.f.u. the slope changes abruptly to about -4 (see Figure 5).

330 Several substitution schemes may explain the incorporation of Ti into phlogopite (Dymek,
331 1983; Henry and Guidotti, 2002; Kogarko et al., 2005):

332 Ti-Tschermak's: $(M^{2+})^{VI}+2(Si^{4+})^{IV}\leftrightarrow(Ti^{4+})^{VI}+2(Al^{3+})^{IV}$ (1)

333 Ti-vacancy: $2(M^{2+})^{VI}\leftrightarrow(Ti^{4+})^{VI}+\square^{VI}$ (2)

334 Ti-oxy: $(M^{2+})^{VI}+2OH^{-}\leftrightarrow(Ti^{4+})^{VI}+2O^{2-}$ (3)

335 Ti-M^{2+}: $2(Al^{3+})^{VI}\leftrightarrow(Ti^{4+})^{VI}+(M^{2+})^{VI}$ (4)

This is the peer-reviewed, final accepted version for American Mineralogist, published by the Mineralogical Society of America.
The published version is subject to change. Cite as Authors (Year) Title. American Mineralogist, in press.
DOI: https://doi.org/10.2138/am-2022-8746. http://www.minsocam.org/

Based on the negative correlation between Ti and Mg+Fe with a slope indicating a 1:1 substitution, we suggest that the Ti-oxy substitution (3) predominates in the analysed micas. By contrast, a correlation with Al or Si is absent, excluding the Ti-Tschermak substitution (1). Consequently, this substitution allows us to calculate the O content of the mica (Ti in a.p.f.u. multiplied by 2), which is equal to 1.74 a.p.f.u. in the most Ti-rich mica from these samples.

The Ti-Tschermak substitution (1) is known to prevail in Mg-rich biotites (XMg>0.65), which is ascribed to misfit between the octahedral and tetrahedral layers (Henry et al. 2005). The Ti-oxy coupled substitution (3) ensures charge balance and it often accompanies the $Ba^{2+}Al^{3+}\leftrightarrow K^{1+}Si^{4+}$ substitution (Figure 6). In the micas from this study two variants of the Ti-oxy substitution (3) occur, where the substitution $Ti^{4+}2O^{2-}\leftrightarrow Fe^{2+}2Cl^{1-}$ links chloroferrokinoshitalite with oxykinoshitalite, and the substitution $Ti^{4+}2O^{2-}\leftrightarrow Mg^{2+}2OH^{1-}$ links phlogopite with oxykinoshitalite. The Ti-oxy substitution (3) is also known from amphiboles (Oberti et al. 1992; Hawthorne et al. 1998).

The Ti-oxy substitution (3) implies incorporation of Ti in the octahedrally coordinated position. This is explained by the strong electrostatic repulsion between Ba^{2+} and Ti^{4+}, which makes the octahedral position more favorable for Ti than the tetrahedral position, which is closer to the Ba^{2+} ions in the interlayer sites. This ultimately leads to the Ti-vacancy substitution (2) or Ti-oxy substitution (3) (Bol et al. 1989).

Substitutions and correlations related to XFe. The covariance diagrams (Figure 5) show a positive correlation of XFe with Ba, Al, and Cl, and a negative correlation of XFe with K and Si. The positive correlation of XFe with Cl, together with the coupled substitution $Ba^{2+}Al^{3+}\leftrightarrow K^{1+}Si^{4+}$ (Figure 6), leads to the formation of the almost pure Cl end member mica, $XFe_{0.88}$, $Ba_{0.95}K_{0.03}Fe_{2.68}Mg_{0.37}Al_{1.91}Si_{2.01}Cl_{1.98}$ (a.p.f.u) with 10.98 wt% Cl, which is close to

chloroferrokinoshitalite with the theoretical formula $BaFe_3Al_2Si_2O_{10}Cl_2$ (Table 2). This is possibly the most Cl-rich mica documented so far from natural samples. The highest Cl content reported to date in micas has been 7.3 wt% Cl (Sharygin et al., 2014) and 4.6 wt% Cl (Léger et al., 1996).

The positive correlation of XFe with Cl has also been documented from other mica occurrences as well as from amphiboles. This is mainly ascribed to the effect that incorporation of Cl is stimulated by the enlargement of the anion site of both minerals with increasing amounts of Fe^{2+} and Al, (and K in the case of amphibole), resulting in a positive correlation of Cl with these elements (Henry and Daigle, 2018; Oberti et al., 1993; Siron et al., 2018).

The relationship between XFe and Ti is more complicated. While micas with relatively low XFe show positive correlation between XFe and Ti. The trend turns to a negative slope when XFe exceeds about 0.4. In addition, micas with low XFe show a positive correlation of Ti with Ba and no correlation of Ti with Cl, while no Ti vs Ba and negative Ti vs Cl correlations are observed in micas with relatively high XFe. These observations are consistent with the fact that for low XFe, the compositional trend phlogopite-oxykinoshitalite is observed, which is characterized by an increase of Ba and Ti and by OH^{1-} to O^{2-} exchange. On the other hand, high XFe compositions cover the compositional range from chloroferrokinoshitalite to oxykinoshitalite with a decrease in Cl, an increase in Ti, and a fairly constant, invariably high Ba content. In conclusion, the observed compositional trends indicate that XFe exerts an important control on the incorporation of Cl or Ti + O in the crystal structure of mica.

Comparison of micas from the matrix and from the MSI. Micas in the matrix are on average enriched in Mg, Si, and K and depleted in Fe, Ba, Cl, and Al compared to micas from MSI. One possible explanation could be that the micas in the matrix were created from different

metasomatic agents with different composition compared to the micas from MSI, which possibly formed during a different evolutionary stage. This is consistent with the fact that fluid heterogeneities may have occured on a millimeter- to centimeter-scale in the subduction environment (Selverstone et al. 1992). In addition, the matrix behaved as an open system, where Cl could be more easily removed during subsequent processes, as compared to the environment in which the MSI formed, which supposedly had more closed system character. The variability of the metasomatising agents is matched by the high variability of the mineral assemblages and the wide range of mica compositions in the MSI. The covariance diagrams (Figure 5) show that some micas in the MSI with lower XFe superpose on the compositional range of the micas from the matrix. If the micas from the matrix and from the MSI were formed from the same fluids/melts, the overlap in the covariation diagrams can be explained by the progressive interaction of a metasomatizing fluid/melt with the rock. It is conceivable that some portion of the fluid/melt formed the MSI with the high Cl content and XFe ratio during the initial stage. The fractions that remained in the matrix for a longer time reacted with the host rock more intensively allowing for the progressive escape of Cl and related decrease in XFe before they were trapped in garnet as MSI during the later stage. Another factor that can potentially explain the observed variability of the mica composition are the small scale compositional heterogeneities in the rocks. This may lead to the formation of local equilibration domains with a variable effective bulk rock composition and induce compositional variations in the fluid/melt during interaction with the surrounding rock.

Possible immiscibility between chloroferrokinoshitalite and oxykinoshitalite. In several cases, two micas with contrasting compositions characterized by the predominance of chloroferrokinoshitalite or of oxykinoshitalite coexist within one MSI (Figure 4i), which is

evident from different contents of XFe, Ti, and Cl (for example: $XFe_{0.20:0.77}$, $Ba_{0.48:0.63}$, $Ti_{0.35:0.02}$, $Cl_{0.27:1.45}$ (a.p.f.u)). This observation suggests the existence of a miscibility gap between chloroferrokinoshitalite and oxykinoshitalite. Distinct compositional trends for Ba, Cl, Ti and XFe can be observed for the mica pairs in the covariation diagrams (Figure 7). However, the coexistence of these micas may also be due to local resetting of the original micas along microcracks. Such microcracks have, however, not been observed and this hypothesis cannot be made unambiguously.

Formation of MSI and the origin of Ba, Cl, and CO_2 rich fluids/melts

It is supposed that the MSI were formed by interaction of mafic lithologies with metasomatic fluid or melt of crustal origin, possibly during interaction with subducting crustal material. The fluid or melt, combined with Mg, Fe, Al, and Cr, was extracted from pyroxenite during metasomatism in a manner similar to the genetically related rocks from the Saxothuringian and Moldanubian Domains (Faryad et al. 2013, Borghini et al. 2018, 2020; Čopjaková and Kotková 2018; Naemura et al. 2018). The fact that the MSI form chains crosscutting garnet crystals and are not correlated with the compositional zoning of garnet indicates that the interaction of the rocks with fluid/melt postdates garnet growth. Fluid or melt probably infiltrated the garnet and clinopyroxene grains along cracks, which were later healed, and the resulting inclusions became isolated. Healing of the cracks indicates that the fluids infiltrated at conditions that were still in the garnet stability field. This led to a closed system behavior and to the effective entrapment of the otherwise mobile Cl. The composition of mica in MSI was controlled by the activities of the species dissolved in the metasomatizing fluid or melt, as described in earlier research (Bol et al., 1989). A different relation between MSI and garnet growth zones than

observed in our study was reported by (Čopjaková and Kotková, 2018), who showed MSI to be systematically concentrated in particular garnet growth zones.

Carbonates from inclusions in ultramafic mantle xenoliths often are interpreted as remnants of solid or melt phases of metasomatic origin. Carbonatitic or alkaline-carbonatitic fluids or melts generated in the mantle may react with mantle minerals to trigger release of CO_2-rich fluids/melts, which may contain a brine component. Therefore it is not strictly necessary to invoke crustal material for the formation of these metasomatizing fluids/melts (Zaccarini et al. 2004; Frezzotti and Touret 2014). This study shows that Ba in the MSI is systematically associated with phases rich in Cl and CO_2, and therefore Ba, like Cl and CO_2, most likely originated from metasomatising fluids/melts. Given the average Ba content of the upper continental crust (~630 ppm, Rudnick and Gao 2014) as compared to the mantle (~7.0 ppm, Sun and McDonough 1989), Ba most likely was derived from subducting crustal material.

The presence of nearly pure end member Cl mica (chloroferrokinoshitalite), Cl-apatite, and locally goryainovite together with carbonates suggests a high Cl and CO_2 activity in the metasomatising fluid or melt. The chemical composition of the micas from the MSI shows that OH is replaced by Cl in the A position in the case of the Fe-rich members and by O in the case of Mg-rich members (XFe>0.5: $OH_{0.01-0.69}Cl_{0.53-1.98}O_{0.01-1.16}$, XFe<0.5: $OH_{0.16-1.87}Cl_{0.02-0.81}O_{0.01-1.74}$; Online Materials Table OM3 in file Supp1). The micas with compositions close to chlorofferokinoshitalite and oxykinoshitalite are therefore effectively anhydrous and the A position is completely occupied with Cl or O. This indicates low a H_2O activity in the metasomatizing fluid or melt, the composition of which may be regarded as silicocarbonatite.

Composition and stability of goryainovite

The crystallization of this rare phosphate with a very high Cl content in the MSI indicates an exceptionally high Cl activity in the fluid or melt. Subsequent decrease in the Cl-activity may have led to its transformation into chlorapatie or perhaps later on to Cl-rich hydroxylapatite, which can often be observed in the matrix.

The composition of goryainovite ($Ca_{1.9–2.0}Sr_{0.0–0.1}(P_{\sim1.0}O_{4.0})Cl_{0.7–0.8}$) shows that Ca is partially substituted by Sr. A similar substitution has been described for apatite (Chakhmouradian et al., 2002; Hughes et al., 1991), but due to the rare occurrence of goryainovite (this work describes its second occurrence so far) the Ca-Sr substitution has not yet been reported for this mineral (Ivanyuk et al. 2017). The missing Cl content that does not correspond to the theoretical Cl content of the ideal goryainovite formula of ($Ca_2(PO_4)Cl$), suggests that the Cl was partially replaced by OH^{-1}.

IMPLICATIONS

This study on Ba-, Ti-, and Cl-rich micas has revealed an extremely high compositional variability between the micas ranging between Ba-rich phlogopite, chloroferrokinoshitalite, and oxykinoshitalite. It has allowed the principal ionic substitution mechanisms to be discerned and shed light on the influence of XFe on the compositional trends. The positive correlation of XFe with Cl has led to the formation of possibly the most Cl-rich mica so far described, a chloroferrokinoshitalite with 10.98 wt% Cl. The coexistence of two micas with distinct compositions close to end member chloroferrokinoshitalite and oxykinoshitalite suggests the presence of a miscibility gap between these two end members.

The occurrence of exceptionally Ba-, Ti-, and Cl-rich micas associated with other Ba- and/or Cl-rich minerals, including celsian, Cl-apatite, and rare goryainovite in the matrix, as well as in garnet and clinopyroxene-hosted MSI, provides important constraints on the composition of melt or fluid involved in syn-orogenetic mantle metasomatism. The prevalence of micas with a low OH content with substantial amounts of Cl or O in the A position, together with carbonates, indicates a high Cl and CO_2 activity and a low H_2O activity in the metasomatizing agent, which most likely was Ba-Cl-rich silicocarbonatitic. The similarity of the MSI, documented in this study, with other MSI in mantle rocks from the Gföhl and the Saxothuringian Domain of the Bohemian Massif gives further insight into a possible common origin and further support the idea that their extended regional occurrence is related to subduction processes during the Variscan orogeny.

ACKNOWLEDGEMENTS

We are very grateful to Ricardo Sallet and the other anonymous reviewer for their constructive comments on the manuscript and suggested corrections that led to the improvement of this paper. We would also like to thank Daniel Harlov for the editorial handling. The work on this contribution was funded by the Austrian Science Fund FWF Project Nr. I 4580-N and Czech Grant Agency grant No.: GACR 20-24210L.

REFERENCES CITED

Ankinovich, S.G., Ankinovich, Y.A., Rozhdestvenskaya, I.V., and Frank-Kamenetskiy, V.A. (1973) Chernykhite, a new barium-vanadium mica from northwestern Karatau. International Geology Review, 15, 641–647.

Becker, H. (1997) Petrological constraints on the cooling history of high-temperature garnet peridotite massifs in lower Austria. Contributions to Mineralogy and Petrology, 128, 272–286.

Blanco-Quintero, I.F., Lázaro, C., García-Casco, A., Proenza, J.A., and Rojas-Agramonte, Y. (2011) Barium-rich fluids and melts in a subduction environment (La Corea and Sierra del Convento mélanges, eastern Cuba). Contributions to Mineralogy and Petrology, 162, 395–413.

Bol, L.C.G.M., Bos, A., Sauter, P.C.C., and Jansen, J.B.H. (1989) Barium-titanium-rich phlogopites in marbles from Rogaland, Southwest Norway. American Mineralogist, 74, 439–447.

Borghini, A., Ferrero, S., Wunder, B., Laurent, O., O'Brien, P.J., and Ziemann, M.A. (2018) Granitoid melt inclusions in orogenic peridotite and the origin of garnet clinopyroxenite. Geology, 46, 1007–1010.

Borghini, A., Ferrero, S., O'Brien, P.J., Laurent, O., Günter, C., and Ziemann, M.A. (2020) Cryptic metasomatic agent measured in situ in Variscan mantle rocks: Melt inclusions in garnet of eclogite, Granulitgebirge, Germany. Journal of Metamorphic Geology, 38, 207–234.

Carswell, D.A. (1991) Variscan high P-T metamorphism and uplift history in the Moldanubian Zone of the Bohemian Massif in Lower Austria. European Journal of Mineralogy, 3, 323–342.

Cesare, B., Acosta-Vigil, A., Ferrero, S., and Bartoli, O. (2011) Melt inclusions in migmatites and granulites. Journal of the Virtual Explorer, 38, 1–21.

Chakhmouradian, A.R., Reguir, E.P., and Mitchell, R.H. (2002) Strontium-apatite: New occurrences, and the extent of Sr-FOR-Ca substitution in apatite-group minerals. Canadian Mineralogist, 40, 121–136.

Cooke, R.A. (2000) High-pressure/temperature metamorphism in the St. Leonhard Granulite Massif, Austria: evidence from intermediate pyroxene-bearing granulites. International Journal of Earth Sciences, 89, 631–651.

Čopjaková, R., and Kotková, J. (2018) Composition of barian mica in multiphase solid inclusions from orogenic garnet peridotites as evidence of mantle metasomatism in a subduction zone setting. Contributions to Mineralogy and Petrology, 173, 1–18.

Dymek, R.F. (1983) Titanium, aluminum and interlayer cation substitutions in biotite from high-grade gneisses, West Greenland. American Mineralogist, 68, 880–899.

Faryad, S.W., Dolejš, D., and Machek, M. (2009) Garnet exsolution in pyroxene from clinopyroxenites in the Moldanubian zone : constraining the early pre-convergence history of ultramafic rocks in the Variscan orogen, 655–671.

Faryad, S.W., Nahodilová, R., and Dolejš, D. (2010) Incipient eclogite facies metamorphism in the Moldanubian granulites revealed by mineral inclusions in garnet. Lithos, 114, 54–69.

Faryad, S.W., Jedlička, R., and Ettinger, K. (2013) Subduction of lithospheric upper mantle recorded by solid phase inclusions and compositional zoning in garnet: Example from the Bohemian Massif. Gondwana Reseach, 23, 944–955.

Ferrero, S., Ziemann, M.A., Angel, R.J., O'Brien, P.J., and Wunder, B. (2015a) Kumdykolite, kokchetavite, and cristobalite crystallized in nanogranites from felsic granulites, Orlica-Snieznik Dome (Bohemian Massif): not evidence for ultrahigh-pressure conditions. Contributions to Mineralogy and Petrology, 171, 1–12.

Ferrero, S., Wunder, B., Walczak, K., O'Brien, P.J., and Ziemann, M.A. (2015b) Preserved near ultrahigh-pressure melt from continental crust subducted to mantle depths. Geology, 43, 447–450.

Filut, M.A., Rule, A.C., and Bailey, S.W. (1985) Crystal structure refinement of anandite-2Or, a barium- and sulphur-bearing trioctahedral mica. American Mineralogist, 70, 1298–1308.

Frezzotti, M.-L., and Touret, J.L.R. (2014) CO2, carbonate-rich melts, and brines in the mantle. Geoscience Frontiers, 5, 697–710.

Frezzotti, M.-L., and Ferrando, S. (2015) The chemical behavior of fluids released during deep subduction based on fluid inclusions†. American Mineralogist, 100, 352–377.

Gayk, T., Kleinschrodt, R., Langosch, A., and Seidel, E. (1995) Quartz exsolution in clinopyroxene of high-pressure granulite from the Munchberg Massif. European Journal of Mineralogy, 7, 1217–1220.

Gnos, E., and Armbruster, T. (2000) Kinoshitalite, $Ba(Mg)_3(Al_2Si_2)O_{10}(OH,F)_2$, a brittle mica from a manganese deposit in Oman: Paragenesis and crystal chemistry. American

554 Mineralogist, 85, 242–250.

555 Grapes, R.H. (1993) Barian mica and distribution of barium in metacherts and quartzofeldspathic
556 schists, Southern Alps, New Zealand. Mineralogical Magazine, 57, 265–272.

557 Guggenheim, S., and Frimmel, H.E. (1999) Ferrokinoshitalite, a new species of brittle mica from
558 the Broken Hill mine, South Africa: Structural and mineralogical characterization. Canadian
559 Mineralogist, 37, 1445–1452.

560 Guy, A., Edel, J.B., Schulmann, K., Tomek, C., and Lexa, O. (2011) A geophysical model of the
561 Variscan orogenic root (Bohemian Massif): Implications for modern collisional orogens.
562 Lithos, 124, 144–157.

563 Hawthorne, F.C., Oberti, R., Zanetti, A., and Czamanske, G.K. (1998) The role of Ti in
564 hydrogen-deficient amphiboles; sodic-calcic and sodic amphiboles from Coyote Peak,
565 California. The Canadian Mineralogist, 36, 1253–1265.

566 Henry, D.J., and Guidotti, C.V. (2002) Titanium in biotite from metapelitic rocks: Temperature
567 effects, crystal-chemical controls, and petrologic applications. American Mineralogist, 87,
568 375–382.

569 Henry, D.J., Guidotti, C.V, and Thomson, J. (2005) The Ti-saturation surface for low-to-medium
570 pressure metapelitic biotites: Implications for geothermometry and Ti-substitution
571 mechanisms. American Mineralogist, 90, 316–328.

572 Henry, D.J., and Daigle, N.M. (2018) Chlorine incorporation into amphibole and biotite in high-
573 grade iron-formations: Interplay between crystallography and metamorphic fluids. American
574 Mineralogist, 103, 55–68.

Hughes, J.M., Cameron, M., and Crowley, K.D. (1991) Ordering of divalent cations in the apatite structure: Crystal structure refinements of natural Mn- and Sr-bearing apatite. American Mineralogist, 76, 1857–1862.

Ivanyuk, G.Y., Yakovenchuk, V.N., Pakhomovsky, Y.A., Panikorovskii, T.L., Konoplyova, N.G., Bazai, A.V., Bocharov, V.N., Antonov, A.A., and Selivanova, E.A. (2017) Goryainovite, Ca2PO4Cl, a new mineral from the Stora Sahavaara iron ore deposit (Norrbotten, Sweden). GFF, 139, 75–82.

Jiang, S.-Y., Palmer, M.R., Li, Y.-H., and Xue, C.-J. (1996) Ba-rich micas from the Yindongzi-Daxigou Pb-Zn-Ag and Fe deposits, Qinling, northwestern China. Mineralogical Magazine, 60, 433–445.

Kamineni, D.C., Bonardi, M., and Rao, A.T. (1982) Halogen-bearing minerals from Airport Hill, Visakhapatnam, India. American Mineralogist, 67, 1001–1004.

Kogarko, L.N., Uvarova, Y.A., Sokolova, E., Hawthorne, F.C., Ottolini, L., and Grice, J.D. (2005) Oxykinoshitalite, a new species of mica from Fernando de Noronha Island, Pernambuco, Brazil: Occurrence and crystal structure. Canadian Mineralogist, 43, 1501–1510.

Kogarko, L.N., Lebedev, V.A., and Levskii, L.K. (2007) Heterogeneity of isotope sources of alkaline magmatism in the hot spot of the southwestern Atlantic: Fernando de Noronha Islands. Doklady Earth Sciences, 412, 85–88.

Kotková, J., O'Brien, P.J., and Ziemann, M.A. (2011) Diamond and coesite discovered in Saxony-type granulite: Solution to the Variscan garnet peridotite enigma. Geology, 39, 667–670.

Kotková, J., Fedortchouk, Y., Wirth, R., and Whitehouse, M.J. (2021) Metamorphic microdiamond formation is controlled by water activity, phase transitions and temperature. Scientific Reports, 11, 1–13.

Kotková, J, Čopjaková, R., and Škoda, R. (2021) Multiphase solid inclusions reveal the origin and fate of carbonate-silicate melts in metasomatised peridotite. Lithos, 398–399, 1–25.

Kullerud, K. (1995) Chlorine, titanium and barium-rich biotites: factors controlling biotite composition and the implications for garnet-biotite geothermometry. Contributions to Mineralogy and Petrology, 120, 42–59.

Kusbach, V., Janousek, V., Hasalová, P., Schulmann, K., Fanning, C., Erban, V., and Ulrich, S. (2015) Importance of crustal relamination in origin of the orogenic mantle peridotite–high-pressure granulite association: example from the Náměšť Granulite Massif (Bohemian Massif, Czech Republic). Journal of the Geological Society, 172, 479–490.

Léger, A., Rebbert, C., and Webster, J. (1996) Cl-rich biotite and amphibole from Black Rock Forest, Cornwall, New York. American Mineralogist, 81, 495–504.

Locock, A.J. (2014) An Excel spreadsheet to classify chemical analyses of amphiboles following the IMA 2012 recommendations. Computers and Geosciences, 62, 1–11.

Lopes, R.P., and Ulbrich, M.N.C. (2015) Geochemistry of the alkaline volcanic-subvolcanic rocks of the Fernando de Noronha Archipelago, Southern Atlantic Ocean. Brazilian journal of geology, 45, 307–333.

Maierová, P., Schulmann, K., Štípská, P., Gerya, T., and Lexa, O. (2021) Trans-lithospheric diapirism explains the presence of ultra-high pressure rocks in the European Variscides.

618 Communications Earth & Environment, 2, 1–9.

619 Manuella, F.C., Carbone, S., Ottolini, L., and Gibilisco, S. (2012) Micro-Raman spectroscopy
620 and SIMS characterization of oxykinoshitalite in an olivine nephelinite from the Hyblean
621 Plateau (Sicily, Italy). European Journal of Mineralogy, 24, 527–533.

622 Medaris, G., Wang, H., Jelínek, E., Mihaljevič, M., and Jakeš, P. (2005) Characteristics and
623 origins of diverse Variscan peridotites in the Gföhl Nappe, Bohemian Massif, Czech
624 Republic. Lithos, 82, 1–23.

625 Medaris, L.G., Beard, B.L., Johnson, C.M., Valley, J.W., Spicuzza, M.J., Jelínek, E., and Mísař,
626 Z. (1995) Garnet pyroxenite and eclogite in the Bohemian Massif: geochemical evidence for
627 Variscan recycling of subducted lithosphere. Geologische Rundschau, 84, 489–505.

628 Medaris, L.G., Ghent, E.D., Wang, H.F., Fournelle, J.H., and Jelínek, E. (2006) The Spačice
629 eclogite: Constraints on the P-T-t history of the Gföhl granulite terrane, Moldanubian Zone,
630 Bohemian Massif. Mineralogy and Petrology, 86, 203–220.

631 Medaris, L.G., Jelínek, E., Beard, B.L., Valley, J.W., Spicuzza, M.J., and Strnad, L. (2013)
632 Garnet pyroxenite in the Biskupice peridotite, Bohemian Massif: Anatomy of a Variscan
633 high-pressure cumulate. Journal of Geosciences, 58, 3–19.

634 Naemura, K., Hirajima, T., and Svojtka, M. (2009) The pressure-temperature path and the origin
635 of phlogopite in spinel-garnet peridotites from the Blanský les Massif of the Moldanubian
636 Zone, Czech Republic. Journal of Petrology, 50, 1795–1827.

637 Naemura, K., Hirajima, T., Svojtka, M., Shimizu, I., and Iizuka, T. (2018) Fossilized melts in
638 mantle wedge peridotites. Scientific Reports, 8, 1–12.

Oberti, R., Ungaretti, L., Cannillo, E., and Hawthorne, F.C. (1992) The behaviour of Ti in amphiboles; I, Four- and six-coordinate Ti in richterite. European Journal of Mineralogy, 4, 425–439.

Oberti, R., Ungaretti, L., Cannillo, E., and Hawthorne, F. (1993) The mechanism of Cl incorporation in amphibole. American Mineralogist, 78, 746–752.

Oen, I.S., and Lustenhouwer, W.J. (1992) Cl-rich biotite, Cl-K hornblende, and Cl-rich scapolite in meta-exhalites: Nora, bergslagen, Sweden. Economic Geology, 87, 1638–1648.

Pattiaratchi, D.B., Saari, E., and Sahama, T.G. (1967) Anandite, a new barium iron silicate from Wilagedera, North Western Province, Ceylon. Mineralogical Magazine and Journal of the Mineralogical Society, 36, 1–4.

Perraki, M., and Faryad, S.W. (2014) First finding of microdiamond, coesite and other UHP phases in felsic granulites in the Moldanubian Zone: Implications for deep subduction and a revised geodynamic model for Variscan Orogeny in the Bohemian Massif. Lithos, 202–203, 157–166.

Petrakakis, K., Schuster-Bourgin, N., Habler, G., and Abart, R. (2018) Ca-rich garnets and associated symplectites in mafic peraluminous granulites from the Gföhl Nappe System, Austria. Solid Earth, 9, 797–819.

Racek, M., Štípská, P., Pitra, P., Schulmann, K., and Lexa, O. (2006) Metamorphic record of burial and exhumation of orogenic lower and middle crust: A new tectonothermal model for the Drosendorf window (Bohemian Massif, Austria). Mineralogy and Petrology, 86, 221–251.

Racek, M., Štípská, P., and Powell, R. (2008) Garnet-clinopyroxene intermediate granulites in the St. Leonhard massif of the Bohemian Massif: Ultrahigh-temperature metamorphism at high pressure or not? Journal of Metamorphic Geology, 26, 253–271.

Rieder, M., Cavazzini, G., Yakonov, Frank-Kamenetskii, V., Gottardi, G., Guggenheim, S., Koval, P., Müller, G., Neiva, A., Radoslovich, E., and others (1999) Nomenclature of the micas. Mineralogical Magazine, 63, 267–279.

Rudnick, R.L., and Gao, S. (2014) Composition of the Continental Crust. Treatise on Geochemistry, 4, 1–51.

Schmädicke, E., Gose, J., and Will, T.M. (2010) The P – T evolution of ultra high temperature garnet-bearing ultramafic rocks from the Saxonian Granulitgebirge Core Complex , Bohemian Massif. Journal of Metamorphic Geology, 28, 489–508.

Schulmann, K., Lexa, O., Štípská, P., Racek, M., Tajčmanová, L., Konopásek, J., Edel, J.B., Peschler, A., and Lehmann, J. (2008) Vertical extrusion and horizontal channel flow of orogenic lower crust: Key exhumation mechanisms in large hot orogens? Journal of Metamorphic Geology, 26, 273–297.

Schulmann, K., Lexa, O., Janoušek, V., Lardeaux, J.M., and Edel, J.B. (2014) Anatomy of a diffuse cryptic suture zone: An example from the Bohemian Massif, European variscides. Geology, 42, 275–278.

Selverstone, J., Franz, G., Thomas, S., and Getty, S. (1992) Fluid variability in 2 GPa eclogites as an indicator of fluid behavior during subduction. Contributions to mineralogy and petrology, 112, 341–357.

Sharygin, V., Kryvdik, S.G., Karmanov, N., and Nigmatulina, E.N. (2014) Chlorine-bearing annite from Khlebodarovka enderbites, Azov Sea region, Ukrainian shield. Mineralogical Journal, 36, 77–94.

Siivola, J., and Schmid, R. (2007) List of Mineral abbreviations. IUGS Subcommission on the Systematics of Metamorphic Rocks, 1–14.

Siron, G., Baumgartner, L., and Bouvier, A.-S. (2018) Significance of OH, F and Cl content in biotite during metamorphism of the Western Adamello contact aureole. Contributions to Mineralogy and Petrology, 173, 63.

Štípská, P., and Powell, R. (2005) Does ternary feldspar constrain the metamorphic conditions of high-grade meta-igneous rocks? Evidence from orthopyroxene granulites, Bohemian Massif. Journal of Metamorphic Geology, 23, 627–647.

Štípská, P., Schulmann, K., and Kröner, A. (2004) Vertical extrusion and middle crustal spreading of omphacite granulite: A model of syn-convergent exhumation (Bohemian Massif, Czech Republic). Journal of Metamorphic Geology, 22, 179–198.

Sun, W., and McDonough, W. (1989) Chemical and isotopic systematics of oceanic basalts: Implications for mantle composition and processes. Geological Society, London, Special Publications 42, 313–345.

Teertstra, D.K., and Sherriff, B.L. (1997) Substitutional mechanisms, compositional trends and the end-member formulae of scapolite. Chemical Geology, 136, 233–260.

Tischendorf, G., Förster, H.-J., Gottesmann, B., and Rieder, M. (2007) True and brittle micas: composition and solid-solution series. Mineralogical Magazine, 71, 285–320.

Tracy, R.J. (1991) Ba-rich micas from the Franklin Marble, Lime Crest and Sterling Hill, New Jersey. American Mineralogist, 76, 1683–1693.

Tumiati, S., Godard, G., Martin, S., Klötzli, U., and Monticelli, D. (2007) Fluid-controlled crustal metasomatism within a high-pressure subducted mélange (Mt. Hochwart, Eastern Italian Alps). Lithos, 94, 148–167.

Whitney, D., and Evans, B. (2010) Abbreviations for Names of Rock-Forming Minerals. American Mineralogist, 95, 185–187.

Zaccarini, F., Stumpfl, E.F., and Garuti, G. (2004) Zirconolite and Zr-Th-U minerals in chromitites of the Finero Complex, Western Alps, Italy: Evidence for carbonatite-type metasomatism in a subcontinental mantle plume. The Canadian Mineralogist, 42, 1825–1845.

715 Figure captions

716 **Figure 1.** Geological map of the Bohemian massif with the area of interest highlighted –
717 granulite massifs Dunkelsteiner Wald and St. Leonhard. Modified after Borghini et al., (2020).

718

719 **Figure 2.** Garnet pyroxenite mineral assemblage. a) Garnet porphyroblast with thin fine-grained
720 symplectitic rim composed of amphibole, plagioclase, orthopyroxene, and spinel in a granoblastic
721 matrix of clinopyroxene. b) Detail of the fine-grained symplectite of amphibole, spinel,
722 plagioclase and orthopyroxene with garnet relict.

723

724 **Figure 3.** Ba(-Cl)-rich mineral phases in the matrix and in clinopyroxene. a) Mica with celsian in
725 a fine-grained symplectite of sapphirine, spinel, orthopyroxene, and amphibole between garnet
726 grains. b) Zoned mica with celsian, plagioclase, and amphibole close to garnet. c) Apatite in the
727 matrix with orthopyroxene and garnet. d) Clinopyroxene containing MSI. e) Detail of MSI
728 comprising apatite, graphite, and mica. f) Clinopyroxene with large amounts of MSI and
729 orthopyroxene lamellae. g) Detail of orthopyroxene lamella associated with mica and apatite.

730

731 **Figure 4.** MSI in garnet. a) Part of a garnet porphyroblast with chains of carbonate-rich
732 inclusions accompanied by MSI. b) MSI containing dolomite, magnesite, apatite, mica, and
733 monazite. c) MSI containing undefined SiO_2 polymorph, dolomite, apatite, clinopyroxene,
734 epidote, and orthopyroxene. d) MSI containing orthopyroxene, scapolite, apatite, monazite, and
735 magnesite. e) MSI containing cordierite, dolomite, and undefined SiO_2 polymorph. f) MSI

containing amphibole, monazite, apatite, and mica. g) MSI with mica, margharite, apatite, clinopyroxene, spinel, scheelite, and celsian. i) MSI of mica, apatite, monazite, and aspidolite. j) Inclusion of goryainovite.

Figure 5. Main compositional trends of Ba(-Cl) rich micas from garnet pyroxenites with respect to XFe and textural position.

Figure 6. Compositional trend corresponding to substitution $Ba^{2+}Al^{3+}\leftrightarrow K^{1+}Si^{4+}$ of Ba(-Cl) rich micas from garnet pyroxenites with respect to the XFe and textural position. TAl is amount of Al in the tetrahedron structural position.

Figure 7. Compositional trends of Cl versus Ba and Ti. Analyses highlighted by the same symbols represent pairs of micas coexisting in one garnet hosted polyphase inclusion potentially indicating the existence of a miscibility gap between oxykinoshitalite and chloroferrokinoshitalite.

This is the peer-reviewed, final accepted version for American Mineralogist, published by the Mineralogical Society of America.
The published version is subject to change. Cite as Authors (Year) Title. American Mineralogist, in press.
DOI: https://doi.org/10.2138/am-2022-8746. http://www.minsocam.org/

752 **Table 1.** Structural formulae of mica end members that can be used for defining the substitutions

753 related to the transition between phlogopite/annite and Ba-micas.

Position:	***I***	M^{VI}	T^{IV}	***O***	***A***
Phlogopite	K	Mg_3	$AlSi_3$	O_{10}	$(OH)_2$
Annite	K	$Fe^{2+}{}_3$	$AlSi_3$	O_{10}	$(OH)_2$
Kinoshitalite	Ba	Mg_3	Al_2Si_2	O_{10}	$(OH)_2$
Fluorokinoshitalite	Ba	Mg_3	Al_2Si_2	O_{10}	F_2
Ferrokinoshitalite	Ba	$Fe^{2+}{}_3$	Al_2Si_2	O_{10}	$(OH)_2$
Oxykinoshitalite	Ba	Mg_2Ti^{4+}	Al_2Si_2	O_{10}	O_2
Chloroferrokinoshitalite	Ba	$Fe^{2+}{}_3$	Al_2Si_2	O_{10}	Cl_2
Anandite	Ba	$Fe^{2+}{}_3$	$Fe^{3+}Si_3$	O_{10}	S(OH)
Chernykhite	Ba	$V^{3+}{}_2$	Al_2Si_2	O_{10}	$(OH)_2$

This is the peer-reviewed, final accepted version for American Mineralogist, published by the Mineralogical Society of America.
The published version is subject to change. Cite as Authors (Year) Title. American Mineralogist, in press.
DOI: https://doi.org/10.2138/am-2022-8746. http://www.minsocam.org/

754 **Table 2.** Representative analyses of Ba-, Cl- and Ti-rich micas (in wt%).

Mineral	Mica												
Position		matrix		MSI in Cpx					MSI in Grt				
Sample	DS072C	DS072C	DS148C	SL-PX-A	SL-PX-A	SL-PX-1-Y	DS025	DS148A	DS148A	DS025-17A	SL-PX-1-Y	SL-PX-1-Y	DL (wt%)
Analyse	Mca-12	Mca-11	Mca-03	Mca-13	Mca-11	Mca-12	Mca-29	Mca-M05	Mca-M40	Mca-21	Mca-60	Mca-65	
P_2O_5	b.d.	b.d.	b.d.	b.d.	b.d.	0.04	b.d.	b.d.	b.d.	b.d.	0.11	0.11	0.03
SiO_2	36.58	32.04	34.66	29.81	30.37	30.05	38.65	25.25	23.53	21.99	20.70	18.93	0.03
TiO_2	4.82	7.10	3.80	5.96	5.76	5.28	1.76	10.01	12.55	8.37	0.05	0.07	0.03
Al_2O_3	17.09	17.52	18.38	16.53	15.29	16.28	21.37	17.05	18.93	17.16	15.43	15.20	0.02
V_2O_3	0.04	b.d.	0.10	b.d.	0.06	b.d.	0.13	b.d.	b.d.	b.d.	b.d.	b.d.	0.02
Cr_2O_3	0.15	0.25	0.43	0.77	0.56	0.34	b.d.	0.08	0.06	0.21	0.02	0.02	0.02
MgO	19.15	15.79	21.15	14.43	13.95	16.10	22.42	12.21	9.16	9.47	5.98	2.34	0.02
CaO	0.04	0.09	0.05	0.21	0.34	0.39	0.10	0.26	0.24	0.30	0.75	0.17	0.01
MnO	b.d.	b.d.	b.d.	0.02	b.d.	b.d.	b.d.	b.d.	b.d.	b.d.	b.d.	0.03	0.02
FeO	5.92	7.28	2.76	9.27	10.79	8.16	3.31	9.44	8.25	12.70	24.99	30.15	0.02
SrO	0.19	0.15	0.12	0.14	0.19	0.16	–	0.20	0.19	0.16	0.83	0.00	0.04
BaO	3.17	10.35	6.59	13.35	12.85	13.87	2.95	19.20	22.27	24.48	21.57	22.76	0.04
Na_2O	0.94	0.64	0.42	0.70	0.45	0.66	0.69	0.40	0.28	0.39	0.13	0.05	0.01
K_2O	7.74	5.37	7.28	3.71	3.91	3.79	4.65	1.89	1.16	0.05	0.61	0.19	0.01
F	b.d.	b.d.	b.d.	b.d.	b.d.	b.d.	b.d.	b.d.	b.d.	b.d.	b.d.	b.d.	0.06
Cl	0.14	0.23	0.36	1.67	2.05	1.33	0.26	0.14	0.69	3.13	10.04	10.98	0.01
total	95.83	96.57	95.75	94.89	94.51	95.12	96.01	95.98	96.61	95.27	91.17	90.02	
	Calculated on 8 cations												
P	0.00	0.00	0.00	0.00	0.00	0.00	0.00	0.00	0.00	0.00	0.01	0.01	
Si	2.73	2.56	2.61	2.50	2.57	2.49	2.81	2.24	2.16	2.09	2.08	2.01	
Ti	0.27	0.43	0.21	0.38	0.37	0.33	0.10	0.67	0.87	0.60	0.00	0.01	
Al	1.50	1.65	1.63	1.63	1.53	1.59	1.83	1.78	2.05	1.92	1.83	1.91	
V	0.00	0.00	0.01	0.00	0.00	0.00	0.01	0.00	0.00	0.00	0.00	0.00	
Cr	0.01	0.02	0.03	0.05	0.04	0.02	0.00	0.01	0.00	0.02	0.00	0.00	
Mg	2.13	1.88	2.37	1.81	1.76	1.99	2.43	1.62	1.26	1.34	0.90	0.37	
Ca	0.00	0.01	0.00	0.02	0.03	0.03	0.01	0.03	0.02	0.03	0.08	0.02	
Mn	0.00	0.00	0.00	0.00	0.00	0.00	0.00	0.00	0.00	0.00	0.00	0.00	
Fe	0.37	0.49	0.17	0.65	0.77	0.57	0.20	0.70	0.63	1.01	2.10	2.68	
Sr	0.01	0.01	0.01	0.01	0.01	0.01	–	0.01	0.01	0.01	0.05	0.00	
Ba	0.09	0.32	0.19	0.44	0.43	0.45	0.08	0.67	0.80	0.91	0.85	0.95	
Na	0.14	0.10	0.06	0.11	0.07	0.11	0.10	0.07	0.05	0.07	0.02	0.01	
K	0.74	0.55	0.70	0.40	0.42	0.40	0.43	0.21	0.14	0.01	0.08	0.03	
F	0.00	0.00	0.00	0.00	0.00	0.00	0.00	0.00	0.00	0.00	0.00	0.00	
Cl	0.02	0.03	0.05	0.24	0.29	0.19	0.03	0.02	0.11	0.50	1.71	1.98	
XFe	0.15	0.21	0.07	0.26	0.30	0.22	0.08	0.30	0.34	0.43	0.70	0.88	

755 Note: Each column represents an individual analysis. – not measured, b.d. below detection limit, DL detection limit.

756

This is the peer-reviewed, final accepted version for American Mineralogist, published by the Mineralogical Society of America.
The published version is subject to change. Cite as Authors (Year) Title. American Mineralogist, in press.
DOI: https://doi.org/10.2138/am-2022-8746. http://www.minsocam.org/

757 **Table 3.** Representative chemical analyses of apatite and goryainovite (in wt%).

Mineral	Apatite										Goryainovite		
Position	matrix			MSI in Cpx			MSI in Grt						
Sample	DS148C	SL-1-X-3	SL-PX-1-Y	DS148C	SL-1-X-3	SL-PX-1-Y	SL-1-X-3	SL-PX-1-Y	DS142C	SL-PX-1-Y	SL-1B-I	SL-1-X-3	DL (wt%)
Analyse	Ap-08	Ap-05	Ap-20	Ap-09	Ap-03	Ap-18	Ap-02	Ap-07	Ap-35	Ap-23	Gor-02	Gor-04	
P_2O_5	41.91	40.73	40.57	41.36	40.28	39.91	40.99	38.02	39.22	39.06	33.11	32.41	0.03
SiO_2	0.18	0.46	0.30	0.27	1.10	0.36	0.55	0.71	0.24	0.87	0.55	0.58	0.04
La_2O_3	–	–	0.41	–	–	0.53	0.20	1.78	0.47	0.58	b.d.	b.d.	0.03
Ce_2O_3	–	–	0.54	–	–	0.62	0.34	1.96	0.44	1.08	b.d.	b.d.	0.02
MgO	0.10	0.15	0.21	0.08	0.77	0.03	0.22	0.15	0.07	0.05	0.28	0.18	0.03
CaO	53.91	52.57	52.47	53.17	50.97	51.11	52.79	47.54	46.96	50.64	55.22	50.59	0.03
MnO	b.d.	b.d.	b.d.	b.d.	b.d.	b.d.	b.d.	b.d.	b.d.	b.d.	b.d.	b.d.	0.06
FeO	0.26	0.21	0.29	0.11	0.20	0.13	0.31	0.58	0.38	0.49	0.54	0.69	0.03
SrO	b.d.	0.93	0.60	0.30	2.20	1.56	2.14	3.35	8.75	2.90	0.44	2.54	0.01
Na_2O	0.06	0.28	0.20	0.10	0.09	0.16	b.d.	0.24	0.12	b.d.	b.d.	0.06	0.06
F	0.91	0.54	0.57	0.27	0.03	b.d.	0.98	0.15	b.d.	b.d.	b.d.	b.d.	0.01
Cl	3.28	3.44	3.60	4.85	6.22	6.50	1.09	5.68	6.54	7.25	12.32	13.38	0.05
total	96.41	95.33	95.59	95.38	95.62	94.40	97.54	94.32	96.64	95.68	90.14	87.05	
	Calculated on 12.5 oxygens										**Calculated on 4.5 O**		
P	3.01	2.98	2.98	3.01	2.94	2.98	2.96	2.92	2.97	2.92	0.97	0.95	
Si	0.02	0.04	0.03	0.02	0.09	0.03	0.05	0.06	0.02	0.08	0.02	0.02	
La	–	–	0.01	–	–	0.02	0.01	0.06	0.02	0.02	0.00	0.00	
Ce	–	–	0.02	–	–	0.02	0.01	0.07	0.01	0.03	0.00	0.00	
Mg	0.01	0.02	0.03	0.01	0.10	0.00	0.03	0.02	0.01	0.01	0.01	0.01	
Ca	4.90	4.87	4.87	4.89	4.72	4.83	4.82	4.62	4.50	4.78	2.05	1.88	
Mn	0.00	0.00	0.00	0.00	0.00	0.00	0.00	0.00	0.00	0.00	0.00	0.00	
Fe	0.02	0.02	0.02	0.01	0.01	0.01	0.02	0.04	0.03	0.04	0.02	0.02	
Sr	0.00	0.05	0.03	0.01	0.11	0.08	0.11	0.18	0.45	0.15	0.01	0.05	
Na	0.01	0.05	0.03	0.02	0.02	0.03	0.00	0.04	0.02	0.00	0.00	0.00	
F	0.24	0.15	0.16	0.07	0.01	0.00	0.26	0.04	0.00	0.00	0.00	0.00	
Cl	0.47	0.50	0.53	0.71	0.91	0.97	0.16	0.87	0.99	1.08	0.73	0.79	
XFe	0.61	0.44	0.43	0.44	0.13	0.68	0.44	0.68	0.75	0.83	0.52	0.68	

758 Note: Each column represents an individual analysis. – not measured, b.d. below detection limit, DL detection limit.

759

This is the peer-reviewed, final accepted version for American Mineralogist, published by the Mineralogical Society of America.
The published version is subject to change. Cite as Authors (Year) Title. American Mineralogist, in press.
DOI: https://doi.org/10.2138/am-2022-8746. http://www.minsocam.org/

760 **Figure 1**

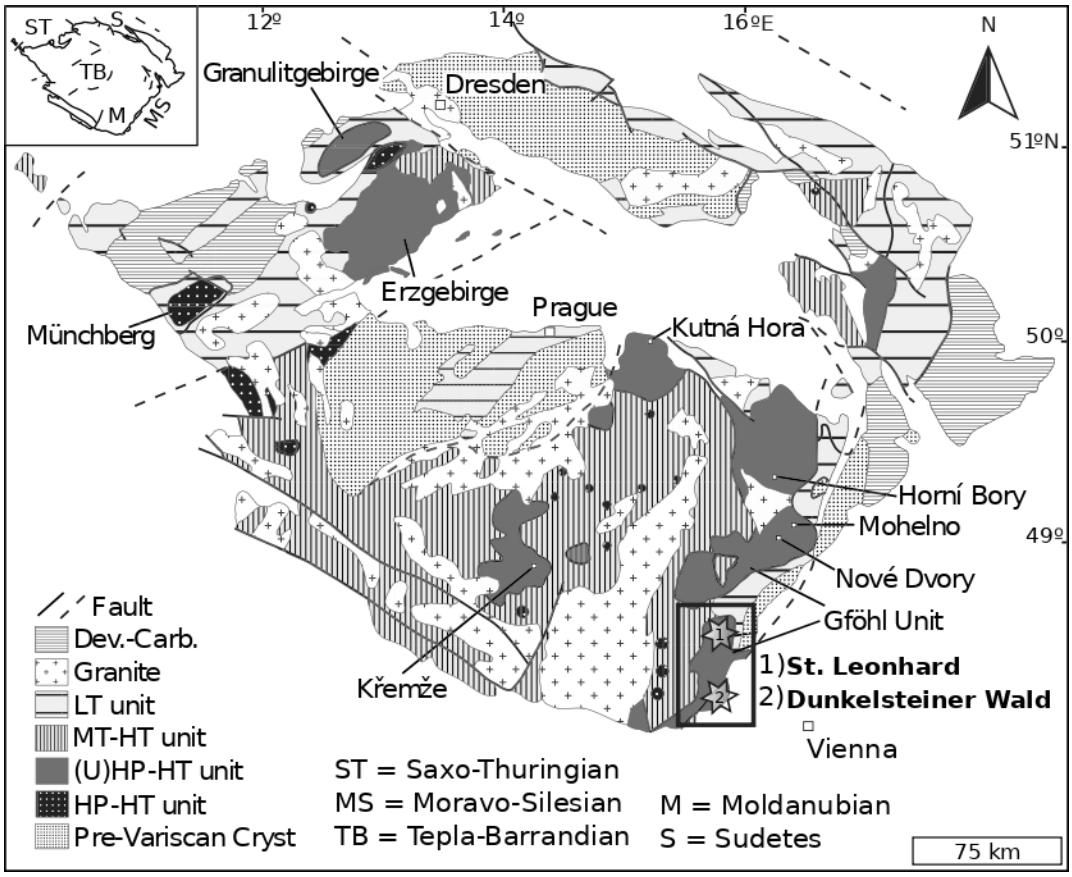

761

762

This is the peer-reviewed, final accepted version for American Mineralogist, published by the Mineralogical Society of America.
The published version is subject to change. Cite as Authors (Year) Title. American Mineralogist, in press.
DOI: https://doi.org/10.2138/am-2022-8746. http://www.minsocam.org/

763 **Figure 2**

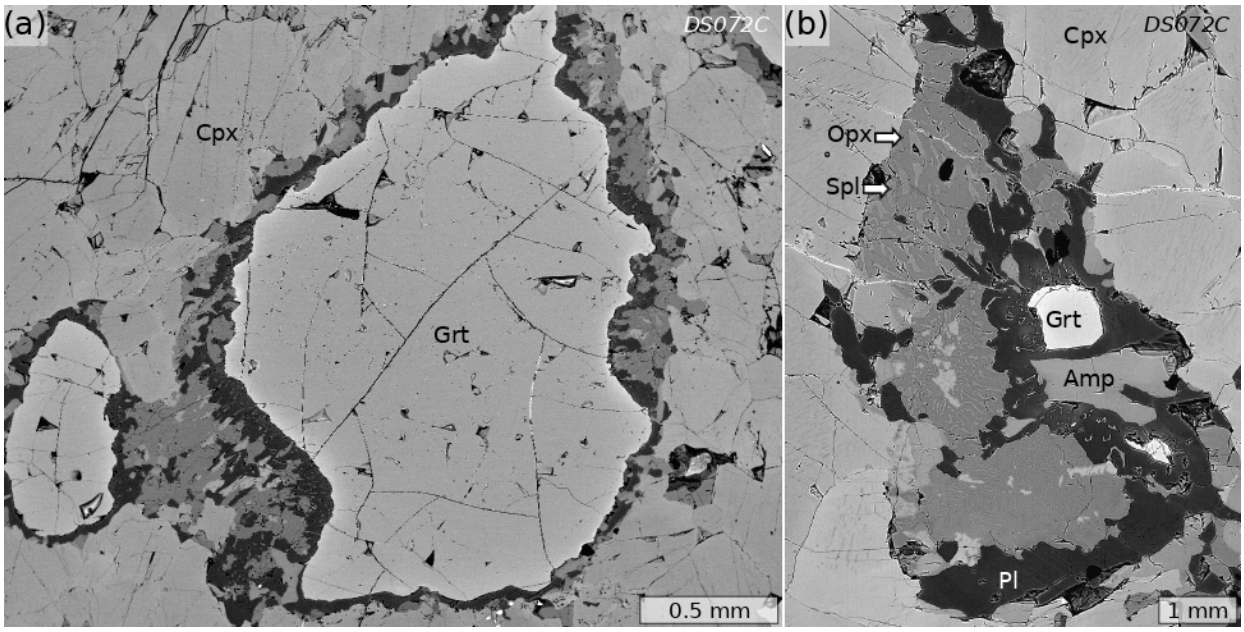

764

765

This is the peer-reviewed, final accepted version for American Mineralogist, published by the Mineralogical Society of America.
The published version is subject to change. Cite as Authors (Year) Title. American Mineralogist, in press.
DOI: https://doi.org/10.2138/am-2022-8746. http://www.minsocam.org/

766 **Figure 3**

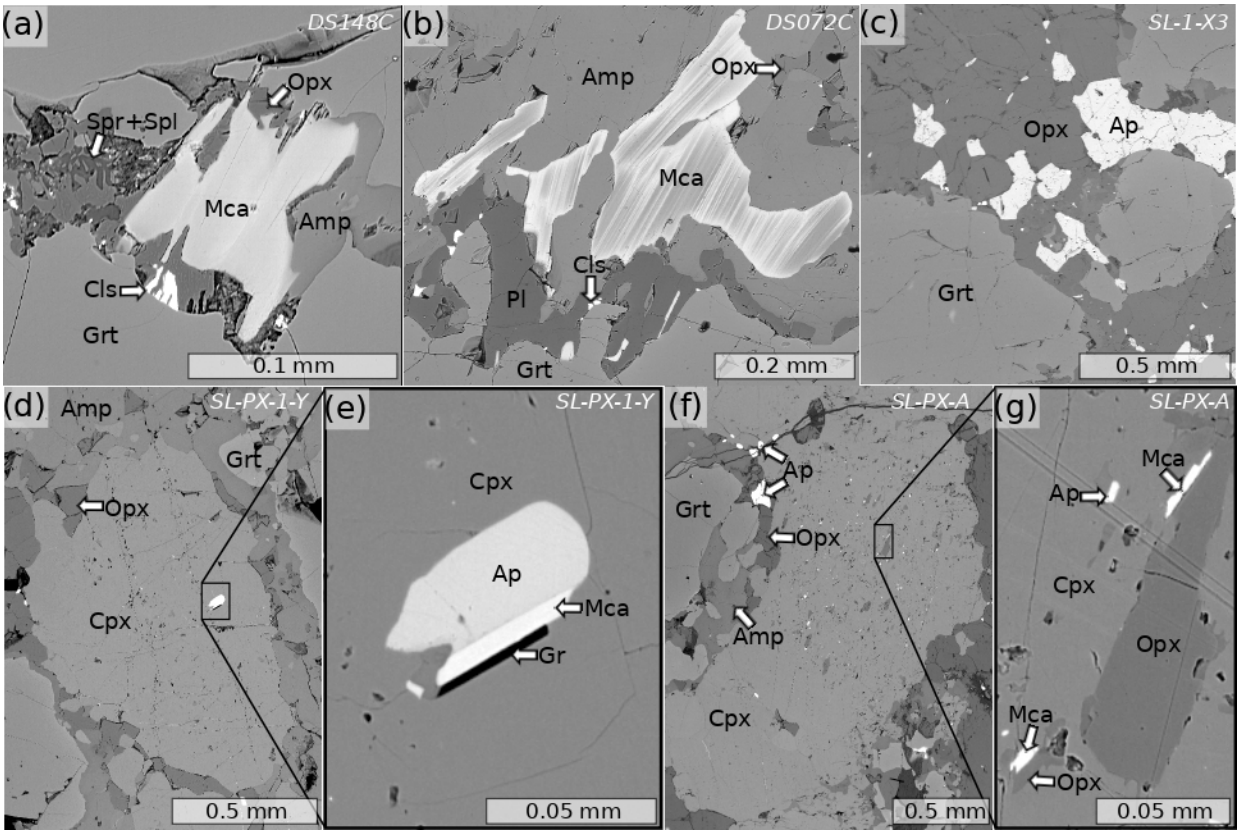

767

768

This is the peer-reviewed, final accepted version for American Mineralogist, published by the Mineralogical Society of America.
The published version is subject to change. Cite as Authors (Year) Title. American Mineralogist, in press.
DOI: https://doi.org/10.2138/am-2022-8746. http://www.minsocam.org/

769 **Figure 4**

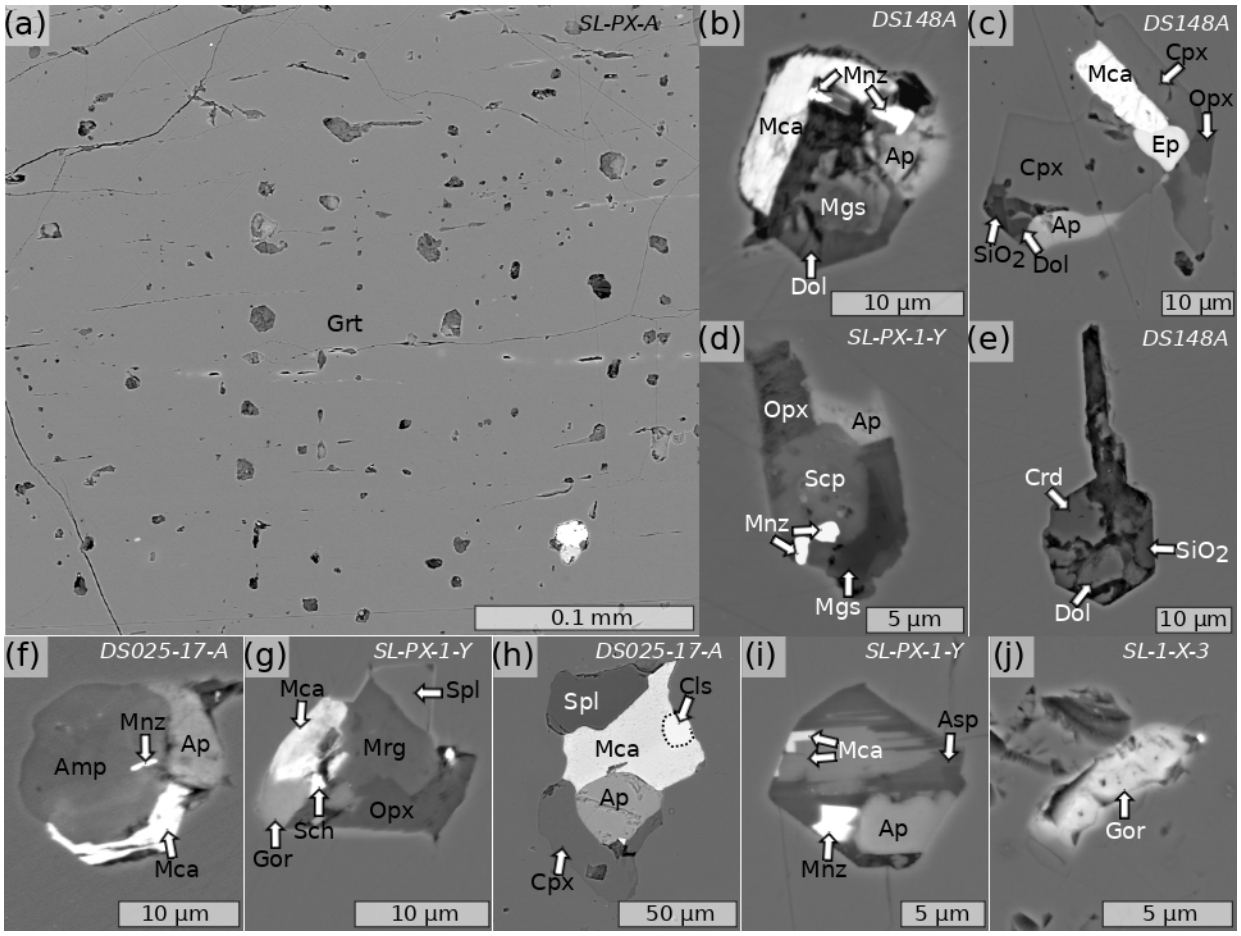

770

771

This is the peer-reviewed, final accepted version for American Mineralogist, published by the Mineralogical Society of America.
The published version is subject to change. Cite as Authors (Year) Title. American Mineralogist, in press.
DOI: https://doi.org/10.2138/am-2022-8746. http://www.minsocam.org/

772 **Figure 5**

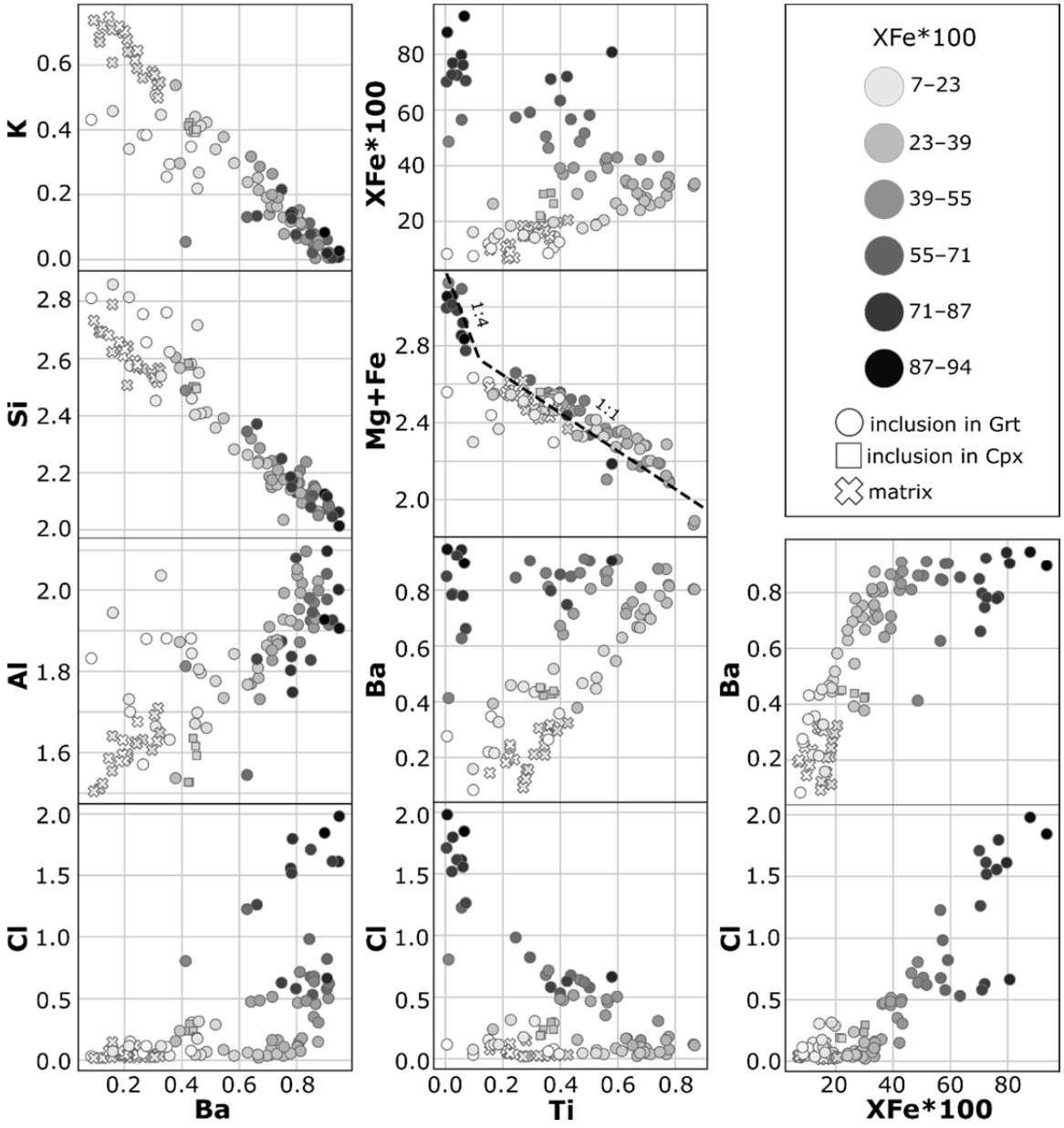

773

774

775 **Figure 6**

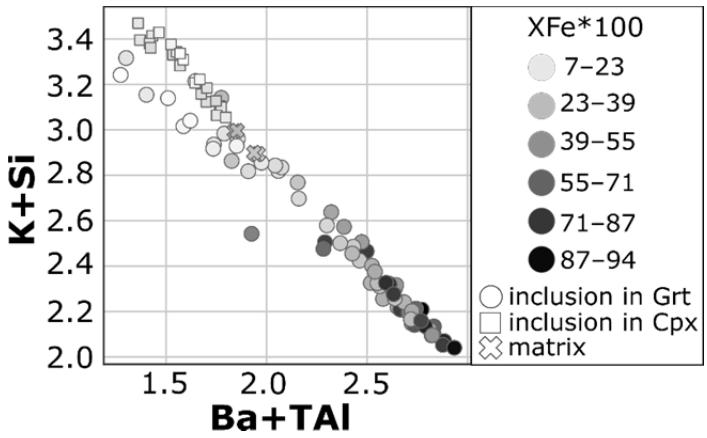

776

777 **Figure 7**

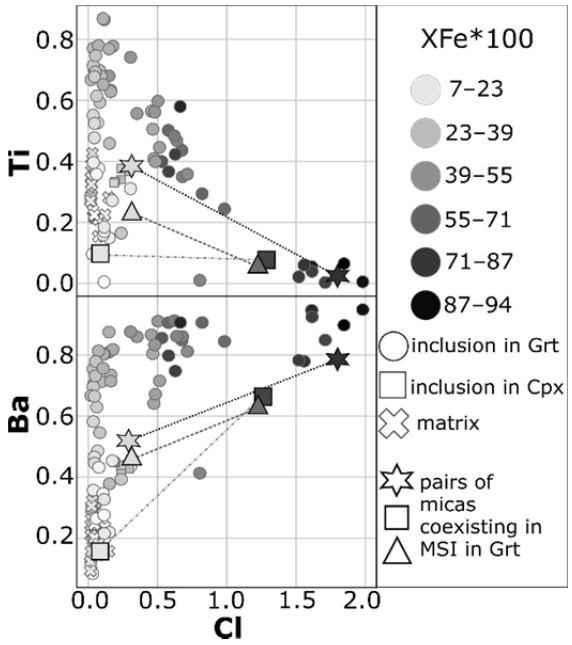

778